CMUG CCI+ Deliverable

Number:	**D2.0g Interim Report Atmospheric Drivers of Ice Sheet Change**
Submission date:	**April 2026**
Version:	**2.2**

Climate Modelling User Group [CMUG]

Deliverable D2.0g

Interim progress report for OWP5.7

Centres providing input: SMHI, DMI

Version nr.	Date	Status
2.0	March 2026	Input from partners
2.1	10 April 2026	Submitted to MetOffice
2.2	28 April 2026	Updated report submitted to ESA

Deliverable D2.0g

Interim progress report

Contents

1. Aim and scope of the deliverable 3
2. Essential Climate Variables - ECV's 3
3. Surface longwave feedback in satellite and EC-Earth data - SMHI 3
4. Evaluation of EC-Earth-PISM coupled system - DMI 5
5. Outlook 14
6. References 14
7. Glossary 15

1. Aim and scope of the deliverable

This OWP5.7 study aims to increase the understanding of atmosphere and surface feedback processes affecting Greenland and Antarctic ice-sheets. We have investigated relations between the ECV's in observations and in the global climate model EC-Earth (https://ec-earth.org/ec-earth/ec-earth3). We have also evaluated the EC-Earth-PISM coupled systems that includes an interactive ice-sheet component. The ECVs are presented in Section 2, relations between land surface temperature and water vapor are investigated in Section 3. Introduction to and results from evaluation of the EC-Earth Ice sheet simulations are presented in Section 4 and the next steps are summarised in Section 5.

2. Essential Climate Variables - ECV's

The ECVs that have been and will be used in this study are listed in the table below. Interactions with the CCI teams have been made during the first phase of this study to learn about the possibilities and limitations of the data, including missing data and screening outliers. More details are provided in the next section. The CCI uncertainty information will be used in the evaluation process when assessing the ECV relationships and calculating metrics.

CCI ECV's	Version	Satellites, timeperiod

Land surface Surface Temperature (LST)	L3S v2.00, 0.05° L3C v3.00, 0.05° L3C v2.00, 0.05°	Multisensor IR, 08/1996-12/2020 MODIS/Terra, 02/2000-12/2018 MODIS/Aqua, 02/2002-12/2018
Water Vapor (TCWV)	L3S v3.2 0.5° L3S v3.2 0.05°, 0.5°	Multisensor MW, 07/2002-12/2016 MODIS/Terra, Land 07/2002-12/2016
Clouds and radiation	L3U, v3, 0.5° L3C, v3, 0.05°	AVHRR-PM, Monthly 1982-2017 AVHRR-PM, daily 1982-2017
Greenland Ice Sheet (GrIS) GMB IV DTU SEC data	v2, 50km v3, 5km	CSR RL06 DTU Space 04/2002-08/2021 1992-2020 https://data.dtu.dk/articles/dataset/
Antarctica Ice Sheet (AIS) GMB, SEC, IV	v3.0, 50km v3.0, 5km	04/2002-07/2020 01/1992-12/2020
Glaciers annual mass changes	0.5°	WGMS-FOG-2023-09 1982-2022

Table 1. Essential Climate Variables (ECVs) release versions, and the satellites and time periods used in this CMUG study.

3. Surface long wave feedback in satellite and EC-Earth data - SMHI

One key objective of OWP5.7 is to evaluate how well global climate models represent land surface temperature (LST) and total column water vapour (TCWV). Cold regions with low humidity including Greenland and Antarctica are warming fast due to the increase in greenhouse gases and feedback processes. Our aim here is to investigate the contribution of the observed and modelled surface longwave feedback to this warming.

In order to determine the longwave surface feedback from the CCI data we derive longwave radiation fluxes from the CCI LST monthly data. We use Stefan Boltzmann law to calculate the surface long wave upward radiation (LWU). The surface longwave downward radiation (LWD) is then calculated from CCI LST and TCWV using the Dilley O'Brian (1998) emissivity formula.

$$DilleyO'BrianEmissivity(LST, TCWV) = 1 - exp(-\tau^{1.66})$$

where

$$\tau = \alpha + \beta\left(\frac{LST}{273.16}\right) + \gamma\sqrt{\frac{TCWV}{25}}$$

$$\alpha = 2.2320, \beta = -1.8750, \gamma = 0.7356$$

$$LWU = \sigma_B LST^4$$

$$LWD = Emissivity * LWU$$

The emissivities determined from the CCI ECVs as a function of water vapor are shown in Figure 3.1 and also the emissivities for the five McClatchey et al (1972) model atmosphere standard cases: Subarctic winter, Mid latitude winter, Sub arctic summer, Mid latitude summer and Tropical. The CCI calculated emissivities compare well with the McClatchey values varying from the lowest values of 0.7 for dry regions up to 0.85 for high humidity regions such as the Tropics. We used the CCI data common available time period 2003-2016. Once the new CCI water vapour data is available we will extend the time period.

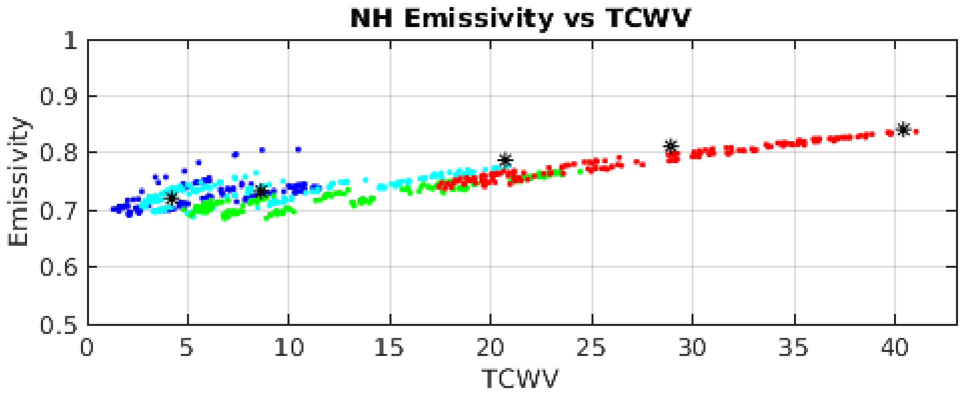

Figure 3.1: CCI Emissivity vs TCWV (kg m^{-2}) for the Northern Hemisphere (NH) land points 2003-2016. The colours show the values for different latitudinal bands (70N-90N, 50N-70N, 30N-50N, 0-30N) and for McClatchey et al 1972 five standard cases (*): subarctic winter, mid-latitude winter, subarctic summer, mid-latitude summer and tropical cases.

Scatter plots of monthly mean TCWV and calculated LWD are shown in Figure 3.2 for the Northern hemisphere for the CCI observations and the EC-Earth global climate model. For the model we used data from the historical 1850-2015 simulation and from scenario SSP585 for the 2016-2100 period. We averaged the CCI and EC-Earth data for the latitudinal bands listed in Figure 3.1.

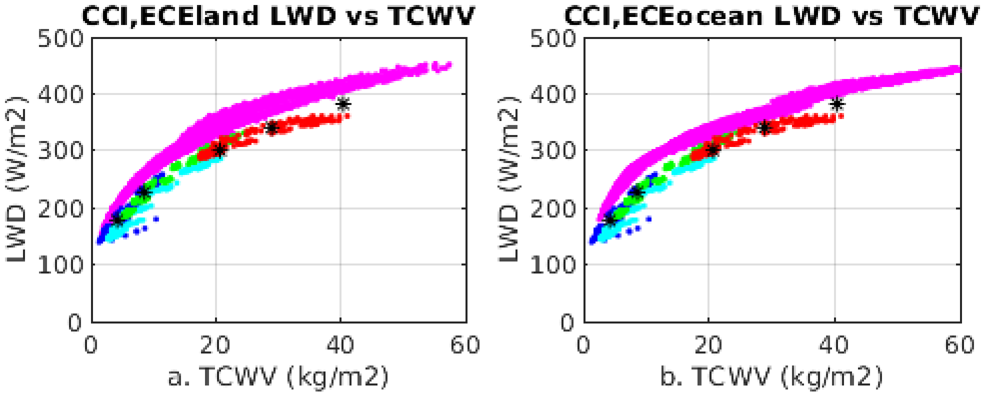

Figure 3.2: Scatterplots of LWD (W/m2) versus TCWV(kg/m2) monthly data for the Northern hemisphere CCI 2003-2016 and EC-Earth SSP585 scenario 2015 to 2100 for **a.** CCI land points (colours as in Fig3, 70N-90N, 50N-70N, 30N-50N, 0-30N) and EC-Earth land points in magneta and **b.** CCI land points (colours as in Fig3) and EC-Earth ocean points also in magneta. The LWD calculated for the McClatchey et al 1972 five standard case are also shown with (*) in both a. and b.

The CCI observational and EC-Earth land data both show similar non-linear relations between LWD and TCWV, with values up to 60kg/m2 towards the end of the century for EC-Earth (Figure 3). The non-linear relations show that the relative increase in LWD is largest for low humidities (<10 kg m^{-2}), which contributes to the fast warming for "dry" regions.

The EC-Earth global model LWD land data are larger than CCI LWD land data calculated from the LST data and larger than the McClatchey LWD data (Fig3.1a). In Figure 3.2b we show the EC-Earth LWD ocean data, that are slightly closer to the CCI values due to the colder ocean than land areas.

Our next step is to investigate why the observed and modelled relations between LWD and TCWV differ. We will re-grid the model and observational data to the same grid before making the latitudinal averages. We will also add the CCI cloud radiation fluxes to the comparisons as well as investigating the water vapour spectral changes using an off-line radiation code.

4. Evaluation of the EC-Earth-PSIM coupled system - DMI

4.1 Context

Another key objective of OWP5.7 is to evaluate how well global climate models represent ice sheet processes. Unlike the regional climate models evaluated using CCI data in previous CMUG work, the EC-Earth-PISM coupled system includes an interactive ice sheet component, enabling evaluation of the full ice mass budget including ice dynamics.

EC-Earth-PISM couples the EC-Earth global climate model with the Parallel Ice Sheet Model (PISM, version 1.2). The coupling operates at the script level with annual exchange of fields: EC-Earth provides monthly surface mass balance (SMB) and subsurface temperature to PISM, while PISM returns updated ice topography, ice extent, and freshwater fluxes from calving and basal melt to EC-Earth (Madsen et al., 2022). PISM is configured on a 5 km regular grid for the Greenland Ice Sheet (GrIS), using the EPSG:3413 polar stereographic projection.

A subset of the output from a historical simulation covering the period 1992–2014 is evaluated here using several CCI ECVs: ice velocity (IV), surface elevation change (SEC), and gravitational mass balance (GMB). These satellite-derived datasets provide independent, spatially resolved observational constraints that allow us to assess both the ice dynamical and surface mass balance components of the coupled model. Additionally, comparisons are made against the BedMachine v5 ice thickness and surface elevation dataset (Morlighem et al., 2017) and the solid ice discharge estimates of Mankoff et al. (2020).

4.2 Comparison against surface ice velocity

The mean PISM surface ice velocity (IV) magnitude (averaged over 1992–2014) is compared with satellite-derived velocities from the CCI IV dataset (Nagler et al., 2015). The IV-CCI data, available at 250 m resolution for the period 2017–2019, was downsampled to the 5 km PISM grid using bilinear interpolation. A land-ice mask was created from the PISM ice thickness field, excluding grid cells with thickness below 3 m to retain only meaningful velocities. We note that the temporal periods differ between model and observations; here we compare the mean velocity fields as representative of the ice flow pattern.

Fig. 3.1 shows the mean velocity magnitude from PISM (left), IV-CCI (middle), and their log-ratio (right). The broad spatial pattern of fast-flowing outlet glaciers and a slow interior is captured by the model. However, the log-ratio map reveals that PISM does not correctly resolve the location of the ice divide, and the Northeast Greenland Ice Stream (NEGIS) is poorly represented, with PISM velocities up to an order of magnitude too high in some areas relative to IV-CCI.

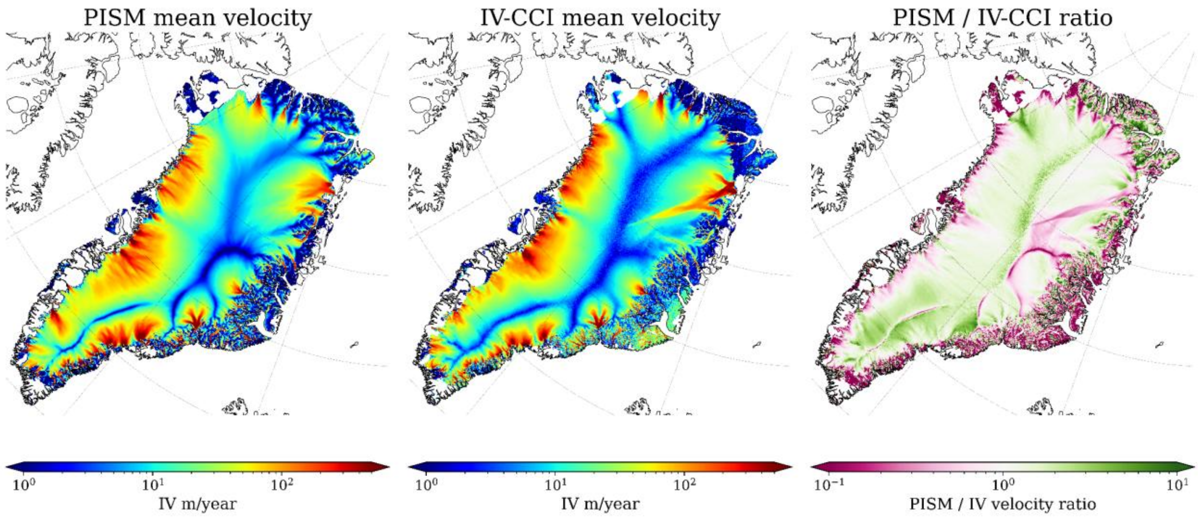

Figure 4.1: Mean surface ice velocity magnitude (left) the EC-Earth-PISM simulation averaged over 1992–2014, (middle) the CCI ice velocity product (IV-CCI; Nagler et al., 2015) averaged over 2017–2019, and (right) the $\log_{10}$ ratio of PISM to IV-CCI velocities. In the ratio plot, white indicates agreement, while green (positive) values indicate regions where PISM overestimates velocity relative to the observations.

The temporal variability and trends in PISM ice velocity are shown in Fig. 3.2. The standard deviation of velocity magnitude (left) highlights the outlet glaciers as regions of highest variability. The linear trend (right) shows modest velocity changes across most of the ice sheet interior, with more pronounced trends near the margins.

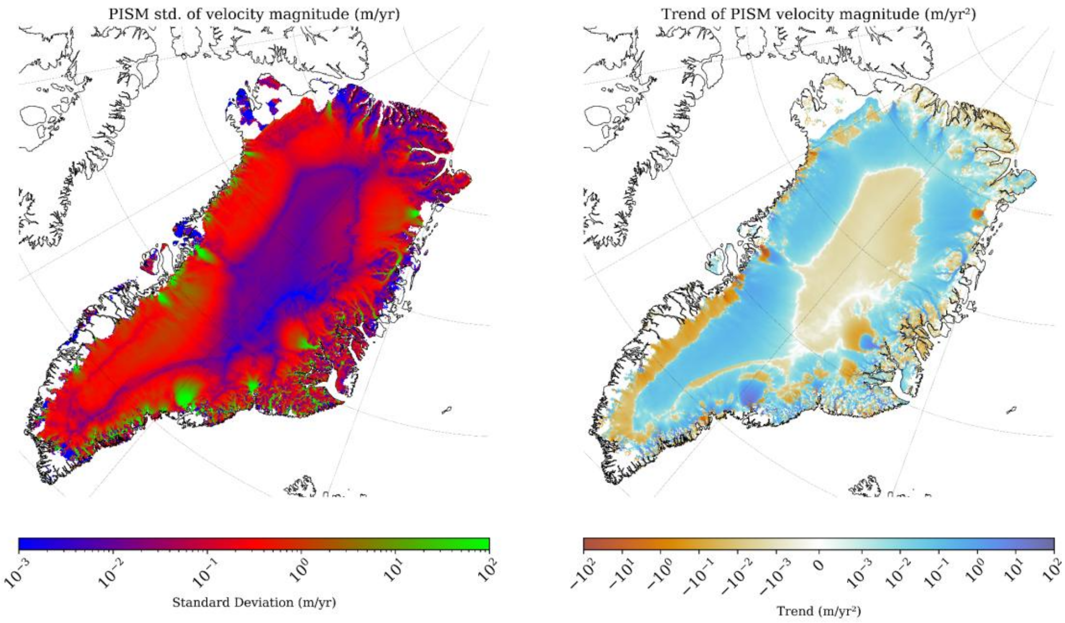

Figure 4.2: Temporal variability and trends in PISM surface ice velocity magnitude over 1992–2014. (Left) Standard deviation of velocity magnitude at each grid point, highlighting outlet glaciers as

regions of highest variability. (Right) Linear trend in velocity magnitude (m yr^{-2}), computed by fitting a linear function to the time series at each grid point.

3.3 Ice thickness and surface elevation

The PISM ice thickness and surface elevation at the end of the simulation (December 2014) are compared against BedMachine v5 (Morlighem et al., 2017). BedMachine provides ice thickness and surface elevation on a 450 m grid, which was interpolated bilinearly to the PISM grid. As BedMachine is a composite product without a single reference epoch, a direct temporal match is not possible; the comparison therefore assesses the overall fidelity of the modelled ice sheet geometry.

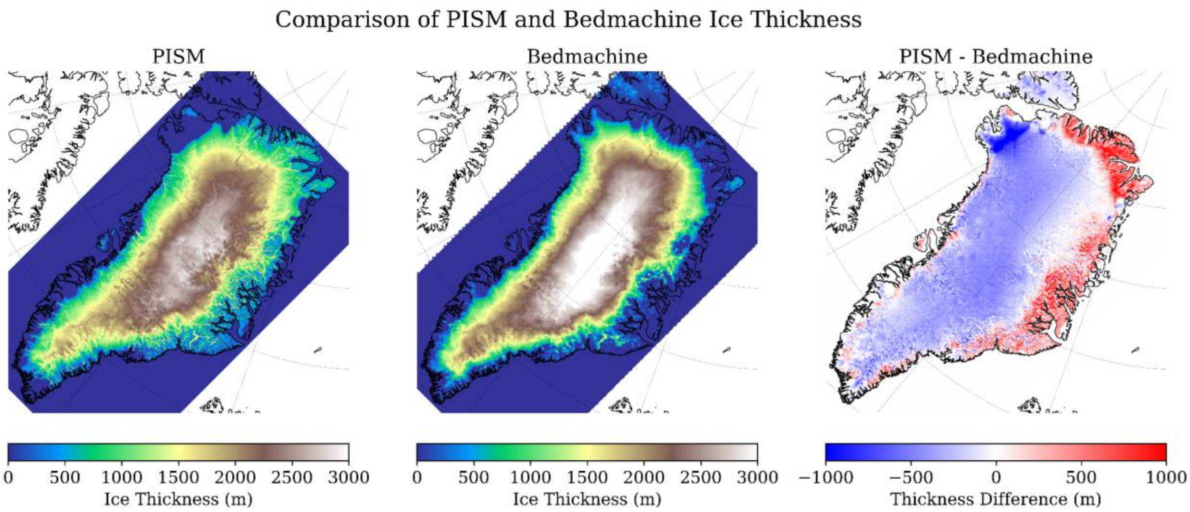

Figure 4.3: Ice thickness over the Greenland Ice Sheet from (left) EC-Earth-PISM simulation (model snapshot December 2014), (middle) BedMachine v5 (Morlighem et al., 2017), and (right) difference. Blue values indicate regions where PISM underestimates ice thickness relative to BedMachine.

Fig. 4.3 compares the ice thickness fields. The large-scale distribution is well captured, but differences of several hundred metres are present, particularly along the margins where PISM tends to underestimate ice thickness. We note that the CCI Digital Elevation Model from GEUS was not used in this analysis, as stitching the 10 m resolution tiles into a complete Greenland mosaic was not feasible within the current timeframe. This comparison is planned for a subsequent phase of work.

4.4 Surface elevation change

Surface elevation change (SEC) data derived from radar altimetry by DTU Space (Simonsen et al., 2020) is used to evaluate the PISM variable representing rate of ice thickness change (referred to as *dlithkdt* in figures). The SEC dataset is provided as 5-year running means; the PISM output was sampled in the same manner to ensure a consistent temporal comparison.

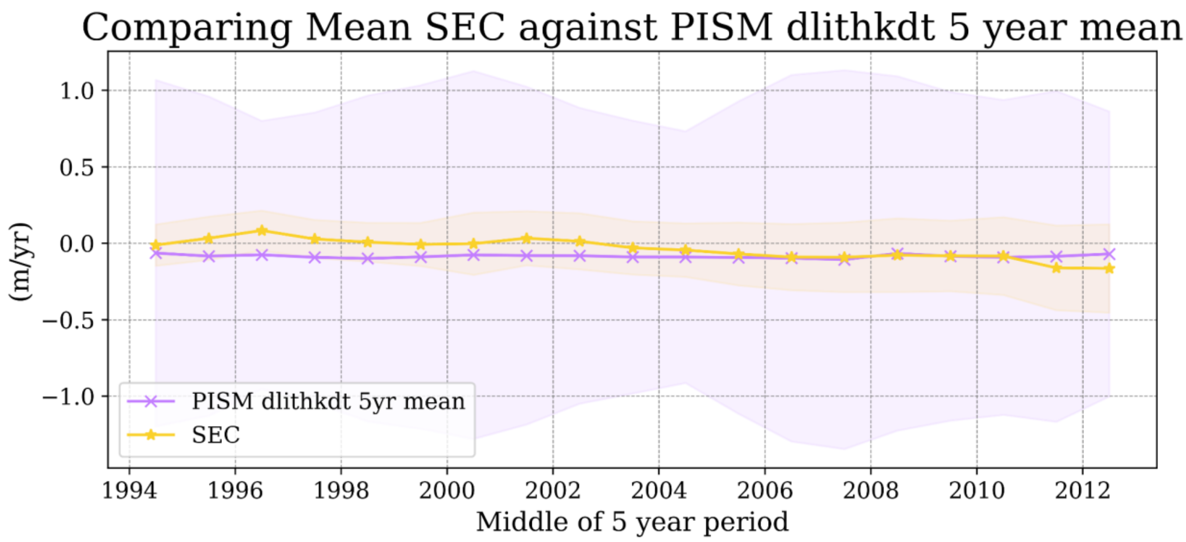

Figure 4.4: Ice-sheet-wide spatially averaged surface elevation change from the CCI SEC product (yellow; DTU Space, Simonsen et al., 2020) and the PISM rate of ice thickness change (*dlithkdt*; purple), both computed as 5-year running means. Shaded regions indicate ±1 standard deviation of the spatial variability within each time step.

The ice-sheet-wide spatial average of both datasets is shown in Fig. 4.4. Both PISM and SEC show surface elevation changes oscillating around zero when averaged over the full ice sheet, but PISM exhibits substantially larger variance. This difference is attributed in part to the spatial and temporal smoothing applied in the satellite SEC processing chain, which reduces high-frequency variability.

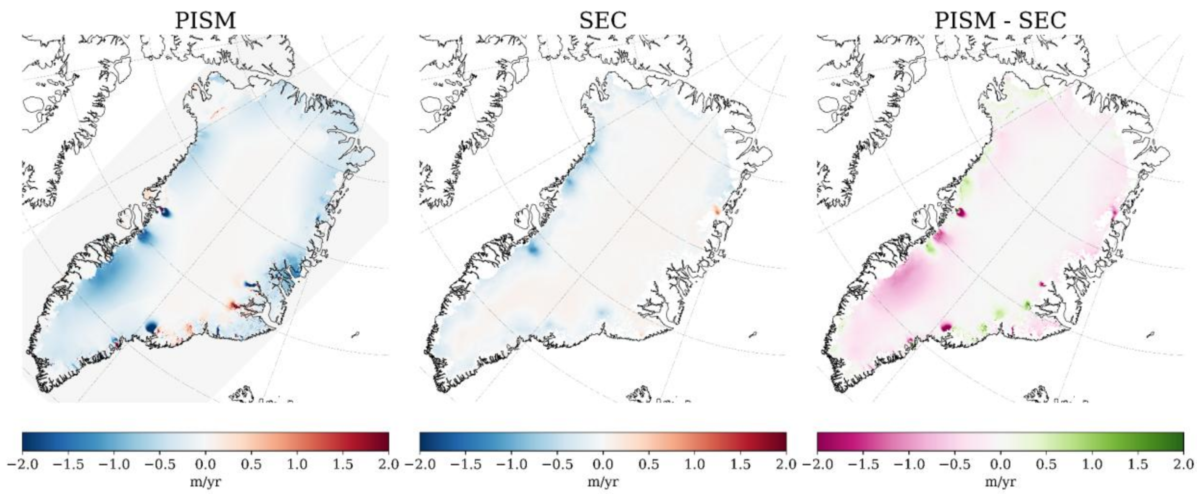

Figure 4.5: Temporal mean (1992–2014) of (left) PISM *dlithkdt* and (middle) satellite-derived SEC over the Greenland Ice Sheet, in m yr^{-1}. (Right) Anomaly map showing the difference (PISM *dlithkdt*

minus satellite SEC). The largest discrepancies are found at outlet glaciers and in the southwest, where surface melt processes are most active.

The temporal mean spatial patterns of PISM and satellite SEC, together with their anomaly (PISM minus SEC), are presented in Fig. 4.5. The largest discrepancies are found at outlet glaciers and in the southwest, where surface melt processes are most active.

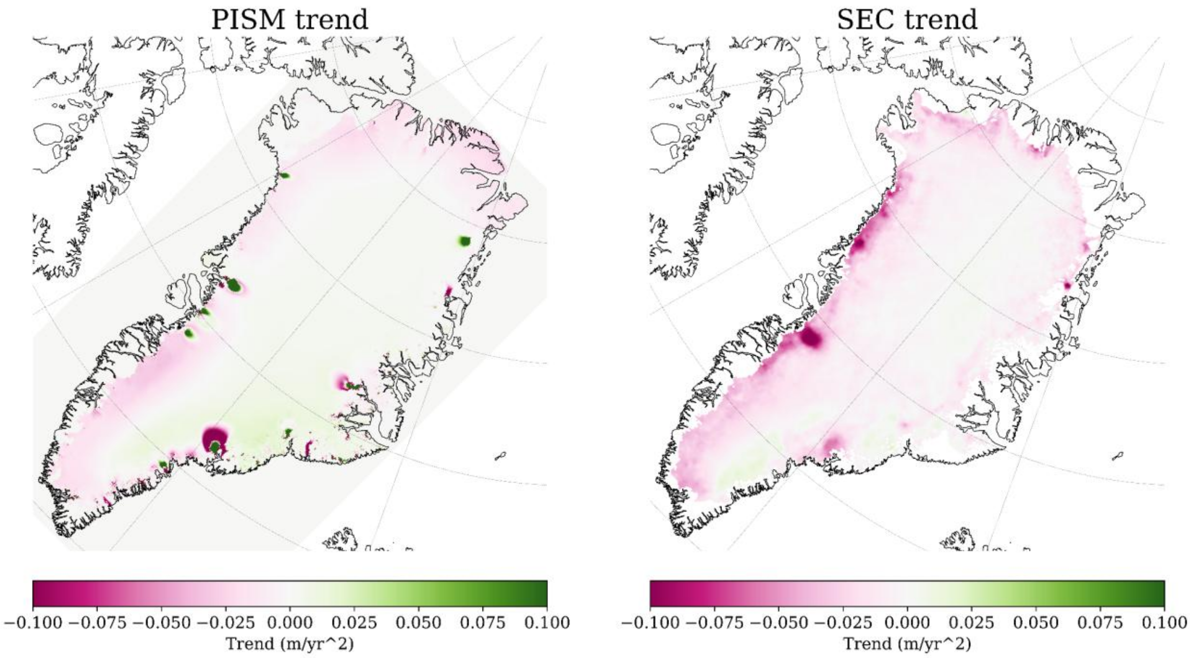

Figure 4.6: Linear trend in (left) PISM *dlithkdt* and (right) satellite SEC over the period of overlap (in m yr^{-2}).

The temporal standard deviation (not shown) confirms that variability is concentrated at the outlet glaciers in both datasets, though more pronounced in PISM. The linear trend maps (see Fig. 4.6) reveal an important discrepancy: while satellite SEC shows a broadly negative trend (surface lowering) that is most pronounced in the southwest, PISM shows a positive trend near the coast at several outlet glaciers. In the accumulation zone of the interior, PISM also shows a more positive trend than observed. These differences point to potential biases in either the atmospheric forcing (SMB from EC-Earth) or the ice dynamical response in PISM, which will be investigated at a later stage.

4.5 Ice discharge

Total ice discharge from PISM is compared with the observational estimates of Mankoff et al. (2020), who combine multiple ice velocity products to derive fly across defined gates around the ice sheet margin. Values from PISM output ("lifmassbf" in figures; in kg m^{-2} s^{-1}) were converted to Gt yr^{-1} at basin scale. This conversion was validated by comparing the (spatially) integrated discharge against PISM time-series diagnostic output to confirm internal model consistency (see Fig 4.7).

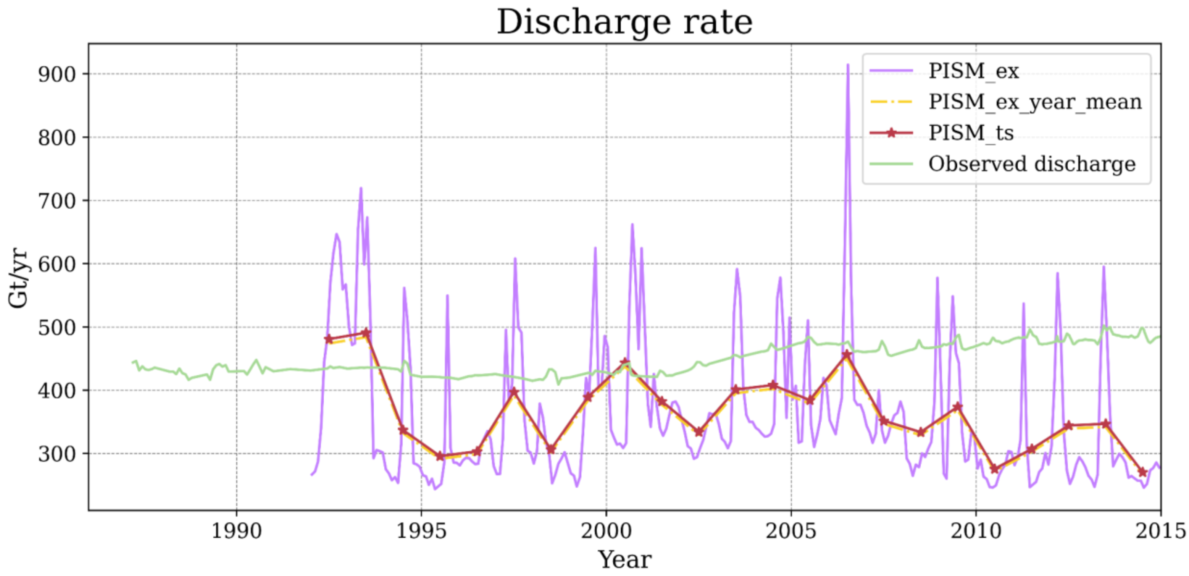

Figure 4.7: Total Greenland Ice Sheet discharge rate (Gt yr^{-1}). Purple: PISM monthly discharge (*lifmassbf*) spatially integrated and converted to Gt yr^{-1}. Orange dashed: same, resampled to annual means. Red: PISM scalar time-series diagnostic (*PISM_ts*), shown to confirm consistency of the spatial integration method. Green: observed solid ice discharge from Mankoff et al. (2020).

The observed discharge rate is approximately constant until around year 2000, increasing then to a higher level by around 2006, and stabilising afterwards. PISM is able to capture the general magnitude of discharge but exhibits significantly more temporal variability (both monthly and annual time scales). This may be related to surge-like behaviour in the model, although this requires further investigation.

4.6 Gravitational mass balance

GRACE and GRACE-FO gravitational mass balance (GMB) data from Döhne et al. (2023) provide a spatially integrated constraint on total ice sheet mass change. The GMB data are spatially resolved and were aggregated following the drainage basin definitions from Mouginot et al. (2019). To enable a valid comparison, the equivalent mass balance output from PISM was constructed from its gridded surface mass balance, basal mass balance, and discharge. This total budget was then validated against the PISM diagnostic variable for total ice mass to confirm internal budget consistency (see Fig 4.8).

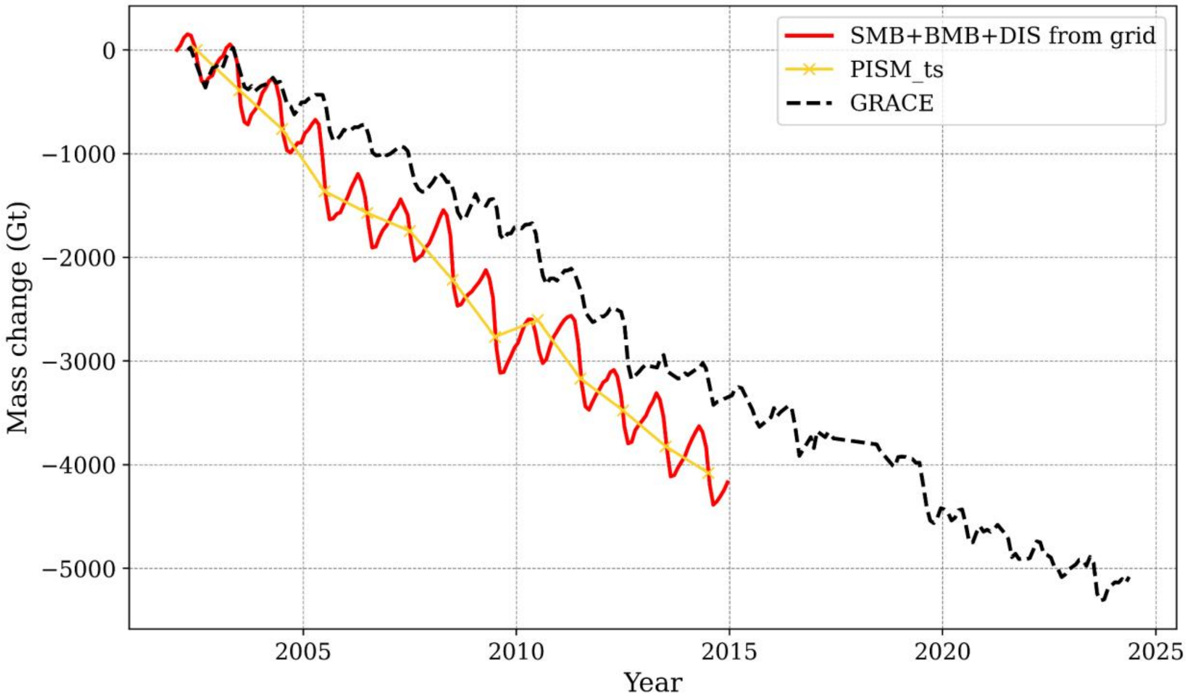

Figure 4.8: Cumulative mass change (Gt) of the Greenland Ice Sheet. Black dashed: Gravitational Mass Balance from GRACE and GRACE-FO (Döhne et al., 2023). Yellow: PISM total ice mass diagnostic (*lim*). Red: PISM mass balance reconstructed from gridded surface mass balance, basal mass balance, and discharge (SMB + BMB + DIS).

At an ice-sheet-wide scale, PISM shows a more negative mass trend than GRACE over the overlapping 2002–2014 period. At basin scales (see Fig. 4.9), we observe significant regional differences. The central-west basin is one of the regions where PISM follows the GRACE trend closely. In contrast, the south-west, north, and north-east basins show more negative trends of mass loss in PISM than in the observational data set, whereas the central-east and north-west basins show the opposite. Interestingly, the south-east basin in PISM initially follows the GRACE trend but eventually diverges from it, reaching a constant state while GRACE continues its negative trend. This divergence might be related to the representation of orographic precipitation on the steep south-east topography in EC-Earth, though this cannot be confirmed at this point and is deferred to future analysis.

4.7 Summary

The CCI ECVs provide useful and independent constraints for evaluating the coupled EC-Earth-PISM system. The comparison reveals that PISM captures the broad spatial patterns of ice velocity, thickness, and surface elevation, but with deficiencies in specific areas. For example, the NEGIS is poorly resolved, outlet glacier dynamics show significant, potentially excessive variability, and the overall mass loss trend is more negative than observed by GRACE. Our regional basin-scale analysis highlights that the biases are not uniform, suggesting that both the atmospheric forcing from EC-Earth and the ice dynamical response in

PISM contribute to the discrepancies. These findings will guide targeted improvements in the next phase of work.

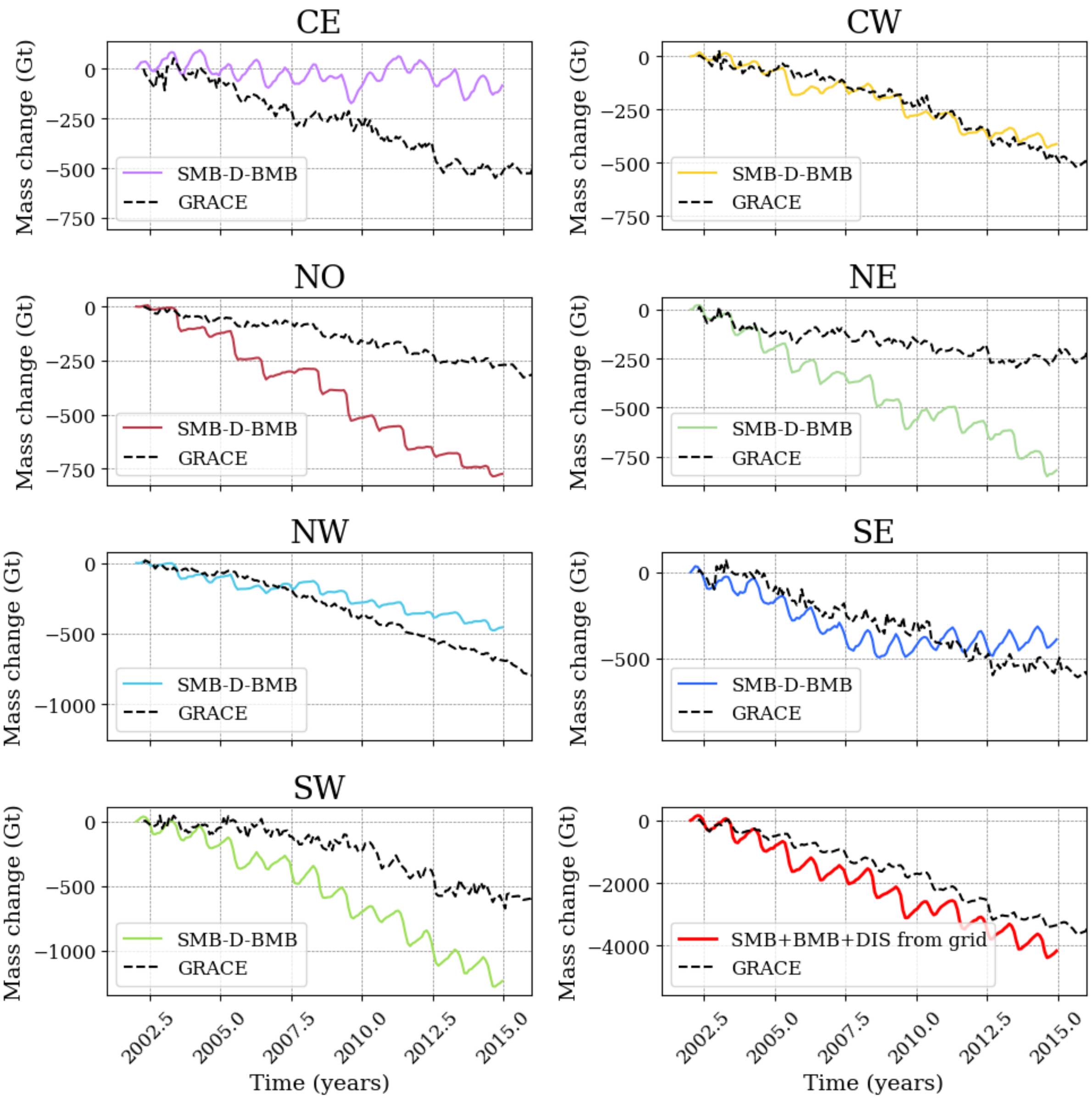

Figure 4.9: Regional cumulative mass change (Gt) for each drainage basin comparing the PISM mass balance (SMB + BMB + discharge; solid lines) with GRACE GMB (Döhne et al., 2023; dashed lines). The bottom-right panel shows the ice-sheet-wide total.

5. Outlook

The integrated water vapor and land surface temperature have been extracted from the global model EC-Earth. Additional global model data from the EU funded projects OptimESM (https://optimesm-he.eu/) and TipESM (https://tipesm.eu/) will be added to this study. The next step at SMHI will be to continue the evaluation of EC-Earth and additional global climate models for the present day, using ESA-CCI and other observational data sets and investigate if they capture the observed variability and the longwave feedbacks. We will update the analysis when new CCI ECV versions are available and also add the CCI Cloud radiation data and the CCI Glaciers regions. DMI will further investigate the EC-Earth PISM surface and energy mass balance for Greenland to understand where and why the coupled models perform the least and most well. The CCI ECV's uncertainty information will also be used in the evaluation process when assessing the ECV relationships and calculating metrics.

6. References

Dilley, A. C., and D. M. O'Brien, 1998: Estimating downward clear sky long-wave irradiance at the surface from screen temperature and precipitable water. Quart. J. Roy. Meteor. Soc., 124A,1391–1401.

Döhne, T., Horwath, M., Groh, A., & Buchta, E. (2023). The sensitivity kernel perspective on GRACE mass change estimates. *Journal of Geodesy*, 97. doi:10.1007/s00190-022-01697-8.

Good, E. J., Aldred, F. M., Ghent, D. J., Veal, K. L., & Jimenez, C. (2022). An analysis of the stability and trends in the LST_cci Land Surface Temperature datasets over Europe. Earth and Space Science, 9, e2022EA002317.

Madsen, M. S., Yang, S., Aðalgeirsdóttir, G., Svendsen, S. H., Rodehacke, C. B., & Ringgaard, I. M. (2022). The role of an interactive Greenland ice sheet in the coupled climate-ice sheet model EC-Earth-PISM. *Climate Dynamics*, 59, 1189–1211. doi:10.1007/s00382-022-06184-6.

Mankoff, K. D., Solgaard, A., Colgan, W., et al. (2020). Greenland Ice Sheet solid ice discharge from 1986 through March 2020. *Earth System Science Data*, 12, 1367–1383. doi:10.5194/essd-12-1367-2020.

Morlighem, M., et al. (2017). BedMachine v3: Complete bed topography and ocean bathymetry mapping of Greenland from multi-beam echo sounding combined with mass conservation. *Geophysical Research Letters*, 44. doi:10.1002/2017GL074954.

Mouginot, J., Rignot, E., Bjørk, A. A., et al. (2019). Forty-six years of Greenland Ice Sheet mass balance from 1972 to 2018. *Proceedings of the National Academy of Sciences*, 116(19), 9239–9244. doi:10.1073/pnas.1904242116.

Nagler, T., Rott, H., Hetzenecker, M., Wuite, J., & Potin, P. (2015). The Sentinel-1 mission: New opportunities for ice sheet observations. *Remote Sensing*, 7(7), 9371–9389. doi:10.3390/rs70709371.

Simonsen, Sebastian Bjerregaard; Sørensen, Louise Sandberg (2020). Greenland Surface elevation change 1992 to present (2024 release). Technical University of Denmark. Dataset. https://doi.org/10.11583/DTU.12866000.v4

Stephens, G. L., M. Wild, J. P. W. Stackhouse, T. L'Ecuyer, S. Kato, and D. S. Henderson, 2012a: The global character of the flux of downward longwave radiation. *J. Climate*, **25**, 2329–2340, doi:10.1175/JCLI-D-11-00262.1.

Stooksbury, D. E., Idso, C. D., & Hubbard, K. G. (1999). The effects of data gaps on the calculated monthly mean maximum and minimum temperatures in the continental United States: A spatial and temporal study. Climate, 12(5), 1524–1533.

5. Glossary

Terms	
Data assimilation	Observations directly influence the model initial state taking into account their error characteristics during every cycle of a model. This is used for reanalysis, NWP, which includes seasonal and decadal forecasting.
Model validation	Observations are compared with equivalent model fields to assess the accuracy of the model. This can be on short time scales for process studies or long time scales for climate trends.
Climate monitoring	This describes the use of a satellite only dataset to monitor a particular atmospheric or surface variable over a period > 15yrs to investigate whether there is a trend due to climate change.
Initialisation	To initialise prognostic quantities of the model with reasonable values at the beginning of the simulation but do not continuously update.
Prescribe boundary conditions	Prescribe boundary conditions for a model run for variables that are not prognostic (e.g. land cover, ice caps etc).
Accuracy	Accuracy is the measure of the non-random, systematic error, or bias, that defines the offset between the measured value and the true value that constitutes the SI absolute standard.
Stability	Stability is a term often invoked with respect to long-term records when no absolute standard is available to quantitatively establish the systematic error – the bias defining the time-dependent (or instrument-dependent) difference between the observed quantity and the true value.
Precision	Precision is the measure of reproducibility or repeatability of the measurement without reference to an international standard so that precision is a measure of the random and not the systematic error. Suitable averaging of the random error can improve the precision of the measurement but does not establish the systematic error of the observation.
Acronyms	
(A)ATSR	(Advanced) Along Track Scanning Radiometer on ERS -1&2 and ENVISAT
AVHRR	Advanced Very High Resolution Radiometer

BADC	British Atmospheric Data Centre
CALIPSO	Cloud-Aerosol Lidar and Infrared Pathfinder Satellite
CCI	Climate Change Initiative
CCMVAL	Chemistry-Climate Model Validation Activity
CDR	Climate Data Record
CMC	Climate Modelling Community
CMIP5	Climate Model Intercomparison Project-5
CMUG	Climate Modelling Users Group
CRG	Climate Research Group
COSP	CMIP5 Observation Simulator Package
CSAB	Climate Scientific Advisory Board
DAAC	Distributed Active Archive Centres
ECV	Essential Climate Variable
EGU	European Geophysical Union
ERA	ECMWF Reanalysis
ERBS	Earth Radiation Budget Satellite
GCOS	Global Climate Observing System
GPS	Global Positioning System
GSICS	GCOS Satellite InterCalibration System
HIRS	High resolution Infrared Radiation Sounder
IGOS	Integrated Global Observing Strategy
IPCC	International Panel for Climate Change
ISCCP	International Satellite Cloud Climatology Project
OSTIA	Operational Sea Surface Temperature and Sea Ice Analysis
PCMDI	Program for Climate Model Diagnosis and Intercomparison
SSM/I	Special Sensor Microwave Imager
SST	Sea Surface Temperature
TCDR	Thematic Climate Data Record